

Results from neutron imaging phase change experiments with LH2 and LCH4

Kishan Bellur^{a,*}, Ezequiel F. Médici^b, Daniel S. Hussey^c, David L. Jacobson^c, Jacob LaManna^c, Juscelino B. Leão^c, Julia Scherschligt^c, James C. Hermanson^d, Chang Kyoung Choi^b, Jeffrey S. Allen^b

^a University of Cincinnati, Cincinnati, OH 45221, United States

^b Michigan Technological University, Houghton, MI 49931, United States

^c National Institute of Standards and Technology, Gaithersburg, MD 20899, United States

^d University of Washington, Seattle, WA 98105, United States

ARTICLE INFO

Keywords:

Cryogenic
Propellant
Condensation
Evaporation
Thin film
Liquid hydrogen
Liquid methane

ABSTRACT

Predicting evaporation and cryo-storage behavior of liquid hydrogen poses a challenge for both terrestrial energy infrastructure and long term space missions. The current understanding of cryogenic phase change and subsequent boil-off is limited, in part, because the values of accommodation coefficients (inputs to phase change models) are still lacking and experimental data to compute them are severely limited. In order to determine the accommodation coefficients, a new cryo/neutron imaging experiment was developed. Tests were conducted in the BT-2 Neutron Imaging Facility at the National Institute of Standards and Technology (NIST) by introducing propellant vapor into cylindrical aluminum (Al 6061) and stainless steel (SS 316) cells placed inside a 70 mm cryostat. Saturation points between 80 kPa - 230 kPa were tested for liquid H₂ and CH₄. Phase change was induced through precise control of pressure and/or temperature. Neutron imaging was used to visualize the liquid and evaporation/condensation rates were determined through image processing. Both hydrogen and methane are perfectly wetting fluids as evidenced by the formation of micro-scale thin film at the onset of condensation and varies in thickness with rate of phase change. The rates of phase change are a function of both the size of the container and the degree of offset from saturation. The unique experimental data, made available through a data repository, have the potential to serve as a bench mark for future studies or serve as a dataset for model validation.

1. Introduction

Given the current state of the world's energy crisis, there is an immediate need for alternative energy sources. Hydrogen is one of the most promising energy carriers. However, there are many technical challenges that remain to be addressed before a hydrogen based energy economy can become viable. Of these, storage and transport of hydrogen remain the most critical [1]. Due to the increased energy density, transport and storage of hydrogen in liquid form is usually favorable. However, liquid hydrogen boils at 21 K under standard atmospheric conditions. Even with multi-layer insulation, liquid-vapor phase change in large cryogenic tanks can lead to significant pressure rise and poses serious constraints to long term storage, transport and stability of the liquid to changes in pressure and temperature. Average daily boil-

off up to 2.2% have been reported [2]. Achieving innovations in storage and transport relies on an improved fundamental understanding of cryogen evaporation.

Liquid-vapor phase change in cryogenic propellants are also of vital concern in long term space missions where zero boil-off is desired [3,4]. CFD models for long term storage and stability of cryogenic propellants are still limited due to the inability to accurately model rate of phase change at liquid-vapor interfaces and capture interfacial thermodynamics [5–7]. These models require accommodation coefficients as inputs and such data is not available. This has reduced the coefficient into a fitting parameter to achieve numerical stability [8].

Ground-based cryogenic experiments with liquid hydrogen have been conducted for over 50 years [9]. These are usually unsteady experiments with complex multi-phase, multi-scale, multi-physics inter-

* Corresponding author.

E-mail address: bellurkn@ucmail.uc.edu (K. Bellur).

<https://doi.org/10.1016/j.cryogenics.2022.103517>

Received 16 February 2022; Received in revised form 14 June 2022; Accepted 22 June 2022
0011-2275/© 20XX

Table 1
Neutron attenuation coefficients for 20 meV neutrons [15].

Species	Density (g/cm ³)	μ (cm ⁻¹)
Hydrogen(liquid)	0.0707	1.43
Hydrogen(vapor)	0.0013	0.02
Aluminum	2.71	0.08
Iron	7.87	0.21
Carbon	2.25	0.56

actions (such as spills [10], sprays [11] and self pressurization [12,13]) that are a challenge to model even for non-cryogenic liquids. These types of tests do not readily allow for measurement of phase change rates or enable the determination of empirical accommodation coefficients. A critical limitation is that conventional visualization techniques cannot be used to image liquids inside metallic containers. To directly address this need, the authors designed and conducted a series of cryogenic propellant liquid–vapor phase change experiments. Evaporation/condensation experiments with hydrogen and methane were conducted at the National Institute of Standards and Technology (NIST) in Gaithersburg, MD at the NIST Center for Neutron Research (NCNR). Tests were conducted in cylindrical and conical containers of various sizes and two different materials. Neutron imaging was used as a non-destructive visualization tool to capture the location, volume and shape of the liquid meniscus inside opaque metallic containers. To the authors' best knowledge, these were the first known neutron images of controlled cryogenic propellant phase change. A prior publication [14] described the motivation behind the tests, relevance to NASA and archived the first ever published neutron images of liquid hydrogen meant as a proof-of-concept. A follow-on manuscript [15] described the neutron imaging setup and associated image processing. These publications briefly described only specific aspects of the experimental setup. A self-contained discourse on the entire experimental setup, procedure and a repository of evaporation/condensation results is still lacking. After the publication of the earlier papers, experiments with methane have been analyzed in addition to hydrogen. The raw data collected has been processed, analyzed and reduced to enable a complete discussion. In this publication, we detail the entire experimental method, setup, analysis and discuss lessons learned throughout the process to aid in repeatability. The first-of-its-kind experimental data is made available through a data repository [16].

1.1. Neutron Imaging

Neutron imaging is a non-destructive radiographic technique similar to X-ray imaging. Both techniques use attenuation characteristics of different elements to enable visualization. The reader is directed elsewhere for an extensive review [17,18] and only a brief introduction to neutron imaging is provided here. When neutrons are incident on a sample, the incident beam could be scattered, absorbed or transmitted. In the case of hydrogen, the scattering crosssection is two orders of magnitude greater than absorption [19]. The intensity of the transmitted beam (I) reduces exponentially with sample thickness (d) as given by the Beer–Lambert law:

$$I = I_0 e^{-\mu d} \quad (1)$$

where, I_0 is the intensity of the incident beam and μ is the attenuation coefficient (dependent on the species of interest and its concentration). The attenuation coefficient for different elements varies with the type of incident radiation and the frequency. X-rays interact strongly with the electron cloud and in general are transparent to light elements but are strongly attenuated by larger elements, such as metals. Neutrons, in contrast, have no charge and hence interact primarily through strong nuclear forces. This enables neutrons to have good penetrating power through heavier elements with large electron clouds (such as

most metals) but strong attenuation by lighter elements (such as hydrogen). This results in a lower value of μ for metals in comparison to lighter elements. Further, density variation between liquid and vapor forms of hydrogen is equivalent to a concentration difference and results in a 2 order magnitude change in μ enabling clear distinction between the two phases. Table 1 compares mass densities and attenuation coefficients of hydrogen, aluminum, iron and carbon.

The difference in attenuation coefficients allows for visualization of hydrogenated liquids in cases where conventional imaging is not possible. Neutron imaging has been used in many applications including but not limited to fluid transport in porous media [20–22], fuel cells [23, 24], and heat pipes [25,26]. Here, the technique is used to image hydrogenated cryogenic propellants - liquid hydrogen and methane.

2. Method

In this section, we detail the fabrication, processing, instrumentation and assembly of the different components of the experimental setup. A bottom-up approach is used. First, each individual component is described followed by assembly and experiment setup. Components that aid in affecting and controlling cryogenic phase change are separated from those used for imaging.

2.1. Test cells

Neutrons are strongly attenuated by the presence of hydrogen and are relatively transparent to metals. Neutron imaging enables the use of opaque metallic test cells and alleviates the need for optical observation windows that are susceptible to leaks. Al 6061 and SS 316 were chosen for the test cells due to their popularity within the cryogenic/NASA community and their readily available thermophysical properties. In order to investigate the effect different materials, container shapes and sizes could have on phase change, multiple test cells were used. The maximum diameter of the test cells were limited by the size of the cryostat bore, which is 70 mm. The minimum diameter of the test cell was limited by a combination of spatio-temporal imaging resolution. The size of the cell changes the shape of the meniscus. Determination of the shape of the liquid–vapor interface was critical to estimating the non-uniform phase change flux that results due to a combination of thermal transport, interfacial curvature, and disjoining pressure. Using hydrogen as the initial target fluid, the diameters were picked such that a range of Bond numbers¹ between 2 and 100 could be tested. The shape of the cells were made to preserve axisymmetry and aid in computational analysis. The preliminary feasibility test with a cell borrowed from NIST suggested a contact angle of 10° for hydrogen [27]. In order to verify this, a hybrid conical cell was devised with a 10° transition slope between two cylindrical sections of diameters 5 and 30 mm. The cells were designed such that a universal flange could be used to seal the top. The test cells are shown in Fig. 1 and listed in Table 2.

The test cells were fabricated from stock material at Michigan Technological University and underwent a multi-step cleaning process. The cells were first immersed in an acid solution made from sulfuric acid (H_2SO_4 , 96% concentration) and hydrogen peroxide (H_2O_2 , 35% concentration) in 3:1 volumetric ratio, respectively for 15 s. After the acid bath, the cells were immediately immersed in a beaker containing distilled water at 363 K. The cells were then immersed in another beaker with distilled water at room temperature. After the final rinse with distilled water, the components were blown with dry nitrogen and sealed in plastic bags. This procedure resulted in a uniform oxide formation and an increase in the surface roughness.

¹ ratio of body force to surface force, $\Delta\rho g r^2/\sigma$, where $\Delta\rho$ is the density difference across the liquid–vapor interface, g is gravitational acceleration, r is the test cell radius, and σ is surface tension.

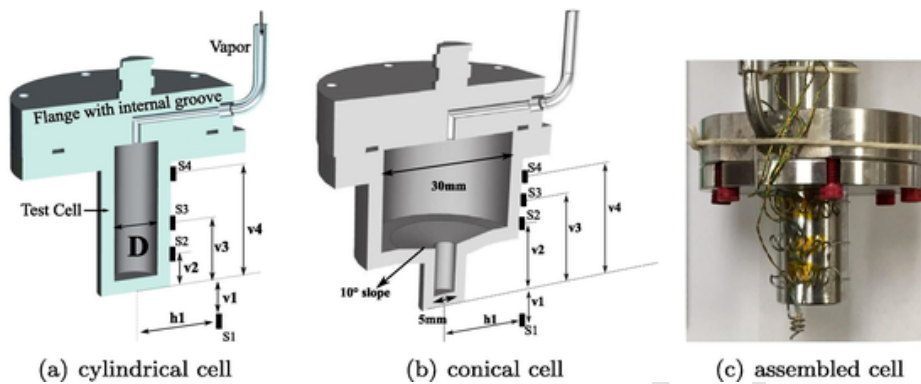


Fig. 1. Two types of cells were used: (a) cylindrical and (b) conical. Two different diameter and materials were used. Si-diode temperature sensors were mounted on the cells at the distances shown. An example of an assembled cell is shown in (c). The cells are attached to a flange that contains an internal groove for an indium O-ring and vapor inlet/outlet.

Table 2

Test cells used in the hydrogen and methane experiments and the sensor locations as indicated in Fig. 1(a). All dimensions are in mm.

Fluid	Cell #	Geometry	Material	D	h1	v1	v2	v3	v4
H2	Tc1	Conical	Al 6061	5/ 30	20	10	5	14	25
	Tc2	Cylindrical	SS 316L	10	20	10	5	12	21
	Tc3	Cylindrical	Al 6061	30	n/a	n/a	7	16	25
	Tc4	Cylindrical	Al 6061	10	20	10	7	14	25
CH4	Tc1	Cylindrical	Al 6061	10	20	10	7	14	25

2.2. Flange

To close the top of the test cell, a flange was fabricated from SS 316. The flange was made to be a universal fit to all test cells. The flange contains an internal groove that houses a indium gasket. The flange was bolted to the cell using 6 anodized Al #4–40 screws. As the screws are tightened, the indium wire deforms and seals the flange/test cell assembly. The flange also has an internal channel that allows for both entry and exit of the vapor. A 1/8 inch male VCR fitting was brazed to the side to allow for connection to a vapor feed line (Fig. 1(a)).

2.3. Sample holder

The test cell and flange assembly was attached to a sample holder (also referred to as the “stick” in prior publications). The sample holder is a hollow SS rod with a 6.35 mm (1/4 inch) outer diameter. The sample holder has multiple baffles to minimize thermal radiation leaks from the test cell to the top flange of the sample holder (Fig. 2). The baffles have staggered holes to insert the vapor feed line and instrumenta-

tion cables. The feed line and cables have separate feedthrough ports on the top flange. The sample holder is spring loaded such that the bottom most baffle makes contact with an annular copper heater housed inside the cryostat (Fig. 3).

2.4. Cryostat

A pumped liquid helium cryostat with a 70 mm bore was used in all the experiments conducted (Fig. 3). The cryostat is a cylindrical device with concentric reservoir rings filled with cryogenic fluids that are undergoing constant vaporization to cool a central sample well. The outermost ring contains a pool of liquid nitrogen evaporating at ambient room pressure, thereby maintaining a constant temperature of 77 K. The second ring is filled with liquid helium. The vaporization of liquid helium occurs by expansion through a throttling valve located at the bottom of the ring. The valve is commonly referred to as a “cold valve” (V1) and is in contact with a copper block containing an embedded heater. Helium vapor travels upward through the innermost ring in contact with the central sample well. The vapor cools the sample well as it rises. At the top of the innermost ring, helium vapor passes through another throttling valve (commonly referred to as the “warm valve”, V2, since it is outside the vacuum insulation jacket) that reintroduces vapor back into the liquid helium reservoir. A secondary link between the helium vapor and liquid reservoir is established through a 3 way valve (V6) where one of the connections is vented to the environment. A helium vapor exhaust valve (V5) can be activated through the 3 way valve (V6) and is only used while refilling liquid helium. All annular rings are enclosed in a vacuum jacket and the sample well extends below the cryostat rings.

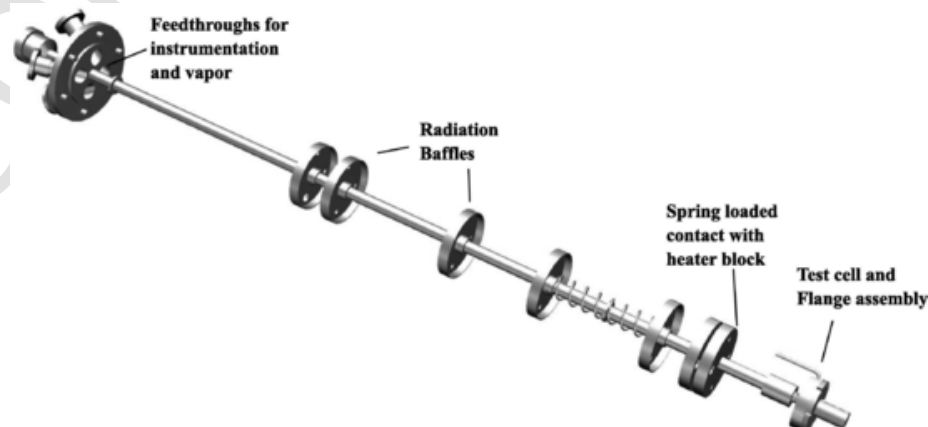


Fig. 2. The sample holder is a long 6.35 mm (1/4 inch) outer diameter, spring loaded hollow rod containing radiation baffles with staggered holes.

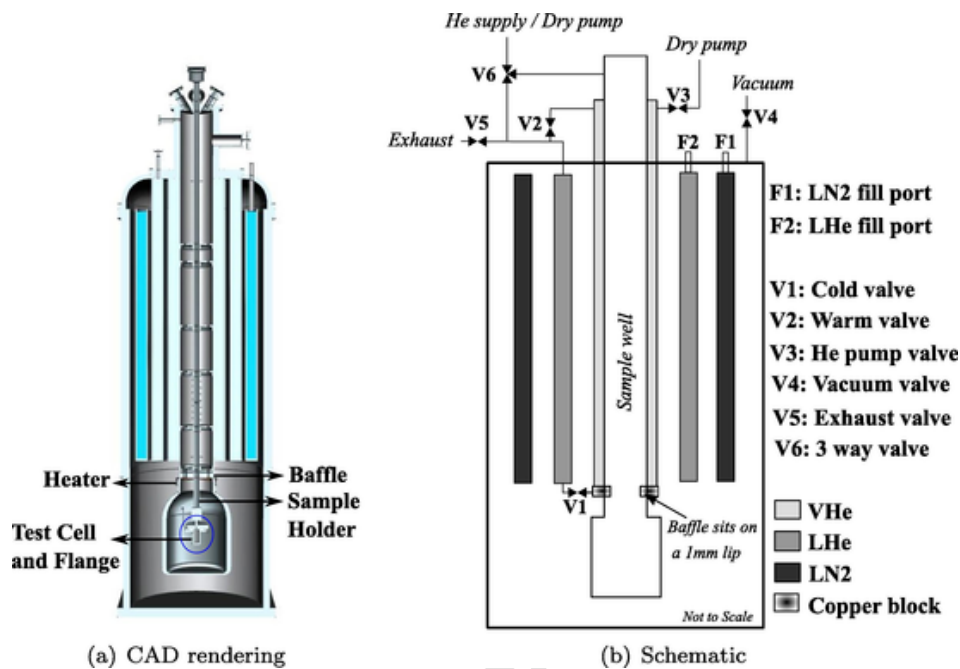


Fig. 3. Cryostat.

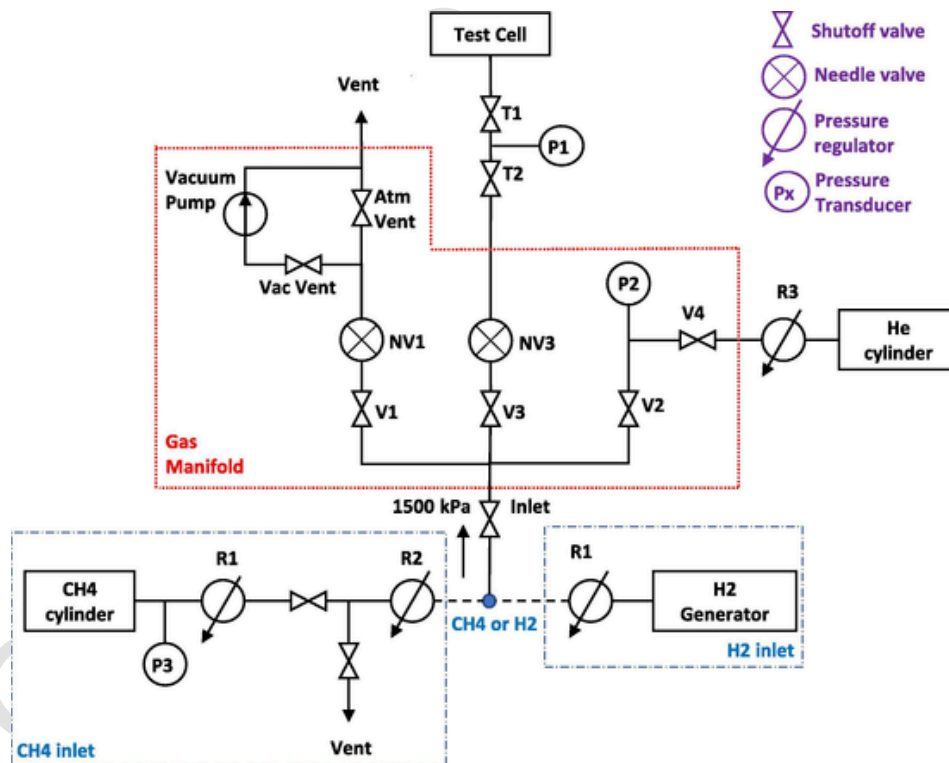


Fig. 4. Schematic of gas manifold and vapor inlets.

The cooling rate is dependent on the temperature of the helium vapor and the vaporization rate. The cooling and vaporization rates are inherently coupled to both the temperature of the copper block that is varied using an embedded resistance heater and the helium vapor pressure varied by a combination of the warm and cold valves. If additional cooling is required, the helium vaporization rate can be increased by pulling a vacuum on the vapor side (V3), but this results in an increased helium consumption and shorter experiment run time. The sample holder is designed such that when inserted into the sample well of the cryostat, the bottom baffle sits on a 1 mm annular ring as part of the

copper block, referred to as a “lip”. A computer aided design (CAD) rendering and a schematic are shown in Fig. 3.

2.5. Assembly

The cleaned test cell and flange was sealed with an indium O-ring and 6 anodized Al 4–40 screws. The mass of each component was measured prior to assembly. The test cell and flange assembly was then mounted to the sample holder. The spring on the sample holder was ad-

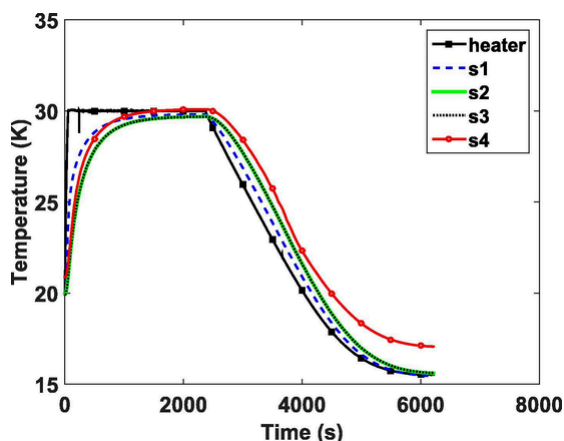
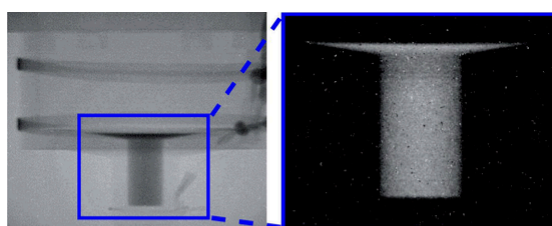
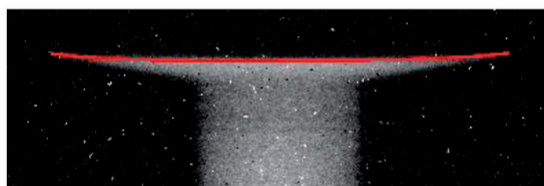


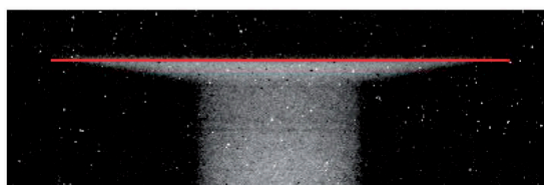
Fig. 5. Temporal variation in temperatures as a result of thermal cycling of the 10 mm Al cell.



(a) Evaporation from the conical cell



(b) Laplace fit with a 2° contact angle



(c) Laplace fit with a 10° contact angle

Fig. 6. Contact angle estimation from conical cell images.

justed so that when inserted into the cryostat, the bottom most baffle makes contact with an annular ring of the copper block. In the methane tests, additional spacers were applied between the sample holder and test cell - flange assembly to increase the spring compression and aid in heater contact.

After installing the test cell and flange on the sample holder, Lakeshore DT-670 SD Si-diode temperature sensors were attached to the test cell. Three sensors were mounted on the outer wall of the test cell held in place by springs custom made from stainless steel wire. The goal was to provide enough tension so that there is direct contact between the sensor and the outer wall. This was necessary to ensure the sensor measures the temperature of the test cell and not the helium transfer gas surrounding it. The temperature of the helium transfer gas was measured by a fourth sensor; suspended vertically downward from the outer edge of the flange (Fig. 1). The sensor cable length was adjusted such that the sensor is approximately 1 cm below the bottom wall of the test cell. The sensor cables from all 4 sensors were enclosed

in shrink tubing. A 1/8 inch SS vapor feed line was attached to the flange using a VCR fitting. The sensor cables and the vapor feed line were then passed through the baffle holes and connected to the top flange of the sample holder (Fig. 3). The tubing was taut to prevent cable damage when the sample holder is inserted into the cryostat.

After component assembly, a helium leak check was performed by pulling a vacuum on the top port of the sample holder that connects to the vapor feedline, flange and the test cell. After a vacuum of approximately 10^{-6} Pa was reached, a small amount of helium gas was sprayed near the vicinity of all connections. If there was a leak in any connection, the helium gas would immediately enter the evacuated space and register a pressure spike. The source of the leak could then be isolated by correlating the location of the spray and the intensity of the pressure spike. The most common source of the leak was the indium seal between the test cell and flange. It was observed that if opposite screws were not tightened sequentially, the deformation of the indium seal was uneven and often resulted in a leak. If a leak was observed at any location, the connection was taken apart and rebuilt. Once the instrumented sample holder passes the leak check, it is ready for insertion into the cryostat.

2.6. Cryostat Preparation

Preparing the cryostat was a multi-step process that involves *vacuum jacket pumping*, *cryogen (re) filling*, *addition of transfer gas*, *cool down* and *sample holder insertion*. In addition to initial setup, some of these tasks were performed multiple times during the course of the experiments.

Vacuum jacket pumping. The outer jacket is evacuated through the vacuum port (V4) and pumped down to approximately 10^{-4} Pa. This step can be skipped if the cryostat was used recently and no problems were encountered.

Cryogen filling. The sample well was evacuated prior to cryogen fill. The 3 way valve (V6) was turned to the UP position such that the sample well could be evacuated to 10^{-4} Pa prior to cryogen fill. Liquid nitrogen was filled through fill port F1. In our experiments, the cryostat was placed inside the NIST BT-2 structure and was not physically or optically accessible during the experiment. Hence, for the duration of the experimental campaign, fill port F1 on the cryostat was instrumented with a long latex hose connection that goes over the walls (ie, beam-stop) and ends in a liquid nitrogen dewar outside the containment structure. The nitrogen fill is completed when the liquid nitrogen overflows from the outer ring. The nitrogen fill was conducted on a daily basis to replenish the mass lost due to constant vaporization.

Liquid helium filling requires the use of double walled, vacuum sealed SS transfer lines and a LHe dewar. First, the exhaust (V5) and the Helium fill (F2) ports were opened. One end of the transfer line was slowly inserted into the helium dewar. This resulted in boil off inside the dewar and subsequent venting of helium vapor from the open end of the transfer line. The open end was inserted into the cryostat LHe fill port. If the transfer pressure reduced during the fill, the transfer line was either be pulled out and reinserted or helium gas at 135 kPa was pumped into the dewar to maintain sufficient pressure for the transfer. The fill was conducted until the helium plume at the exhaust port turned white indicating liquid exhaust. Once the fill was complete, the fill port and the exhaust port were closed.

Addition of transfer gas. An evacuated sample well poses several issues due to lack of a conduction and convection. Under a vacuum, the temporal response to a temperature change is tremendously slow and there exists a significant temperature gradient within the sample well. Each solid-solid contact (baffle-to-copper block, baffle-to-sample holder rod, sample holder rod-to-flange, flange-to-test cell, etc) offers a resistance to conduction heat transfer. In order to aid in heat transfer from the heater block to the test cell, a small amount of helium transfer gas was added after the sample well had been evacuated. This gas penetrated the spaces between the solid-solid contacts and reduced the con-

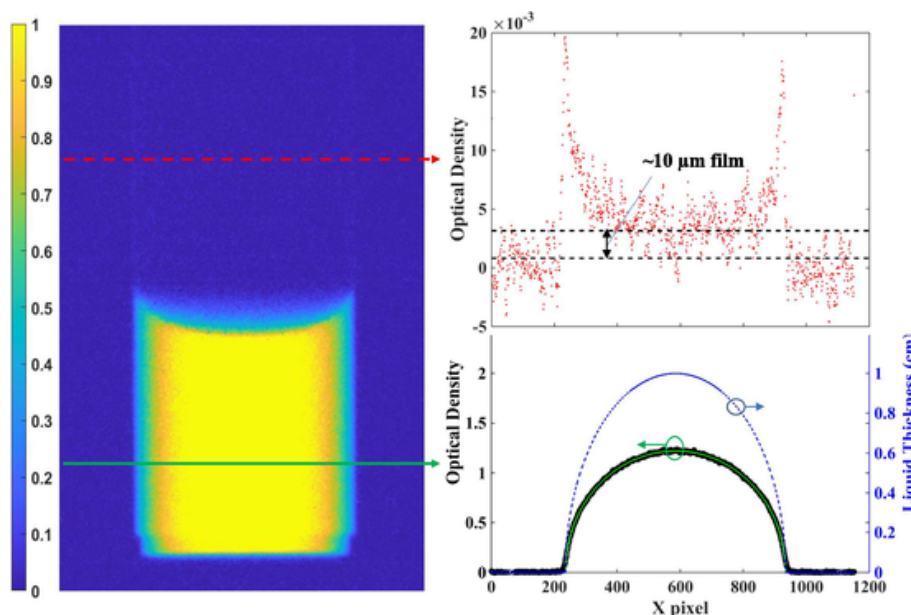


Fig. 7. Optical Density image of hydrogen in Tc4 at 21 K and determination of film thickness.

tact resistances. This also aided in conductive (and convective) heat transport through the vapor itself and significantly reduced the time to achieve thermal equilibrium. Approximately 1.2 m length of 6.35 mm (0.25 inch) latex tubing filled with helium gas at 135 kPa was added to the evacuated sample well. The exact amount was not measured in the hydrogen campaign and likely varied with each test cell but the resulting pressure in the sample well was estimated to be 400 Pa to 700 Pa. At the end of the methane experimental campaign, it was experimentally verified to be 600 Pa.

Cooldown. Once the cryostat was filled with cryogenics, the sample well evacuated and the helium transfer gas added, the cryostat is cooled down from room temperature to a base temperature. The cold (V1) and warm (V2) valves were adjusted to achieve the desired cooling rate. A quarter turn of the cold (V1) valve and 3 turns on the warm (V2) valve yielded the best combination for thermal control. At this setting, the cryostat took 12–24 h to reach base temperature (20 K for hydrogen and 90 K for methane). For enhanced cooling, the innermost helium ring could be connected to a dry roughing pump via V3. This increases vaporization rate and subsequent cooling at the cost of increased helium consumption.

Sample holder insertion. A sample holder (and test cell) swap was possible while the cryostat was still in its base operating temperature. The process of removing or inserting a sample holder was the same. The 3 way (V6) valve was moved to the Helium supply position and the sample well was flooded with gaseous helium till the top flange just floats against the gas pressure. At this point, the top flange was removed and the sample holder was carefully inserted (or removed) under a constant flow of helium gas. As soon as the new sample holder was secured, the sample well was evacuated. The process was completed as quickly as possible to minimize air entrainment. The vacuum and helium purge cycles were repeated at least twice to ensure no trace gases are present in the sample well. After the final purge, the sample well was evacuated, the 3 way valve (V6) was closed and the instrumentation cables were connected via feedthrough ports.

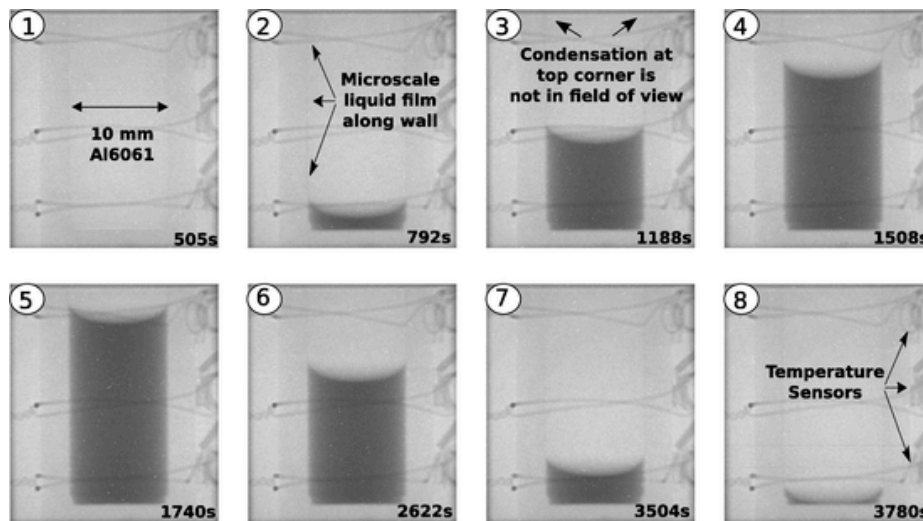
2.7. Instrumentation and control

The copper block at the base of the helium reservoir is the primary thermal control in the cryostat. The copper block houses a resistance heater with an embedded temperature sensor (NTC RTD X45720) and is in contact with the cold valve. Temperature control of the copper block

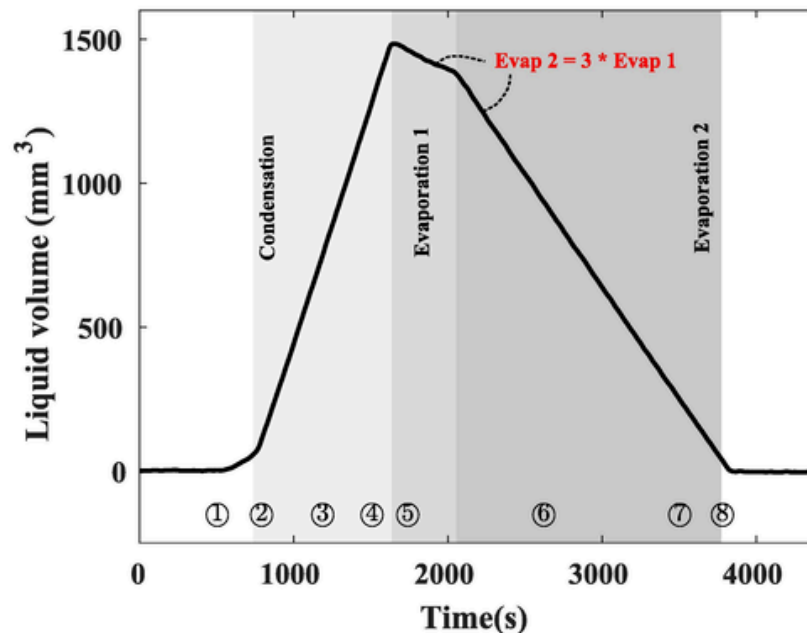
is achieved by matching the evaporative cooling power of helium with the heater power applied to the resistance heater. The cooling power can only be controlled manually (primarily through the cold and warm valves) and is usually set prior to the start of the experiment. Since the cryostat is placed in the path of a neutron beam, active tuning of the cold and warm valves (V1 and V2, respectively) was not possible. Therefore, the temperature was controlled by actively varying the heater power. The heater and copper block temperature sensor was connected to a Lakeshore model 331 controller. PID control was implemented to actively vary the heater power to obtain the set point temperature using the “auto tune” feature of the Lakeshore model 331 controller. Setting the temperature in the copper block was only an intermediate step with an ultimate goal to control the temperature of the test cell. The copper block served as the thermal mass that was then used to transfer heat to the sample well and finally the test cell via multiple heat transfer modes described in a later section.

In order to effectively control rate of phase change, active control of vapor pressure was necessary. In addition, to set up a clean sample environment devoid of contaminants, the chamber must be evacuated and leak checked extensively prior to introduction of the sample vapor (H₂/CH₄). To achieve these tasks a custom manifold was set up as shown in Fig. 4. The manifold was built such that 3 tasks can be performed: (1) evacuate the test cell and vapor line, (2) purge with helium gas, and (3) introduce cryogen vapor into the test cell and accurately control the vapor pressure. A vacuum pump and compressed helium gas cylinder attached to the manifold allowed for evacuation and purge respectively. The hydrogen inlet consisted of a hydrogen generator while the methane inlet consisted of a compressed gas cylinder. Pressure control was achieved by a combination of valves as discussed in Section 3.2.

Cryostat leak tests. To ensure that the test cell was completely isolated from the sample well, both vacuum and pressurized helium leak tests were conducted. Vacuum test involved evacuating the test cell via the vacuum pump attached to the manifold with inlet valve closed. For the pressurized test, helium gas was introduced into the test cell and the pressure was increased to above atmospheric pressure with V1 and inlet valve closed. The change in pressure with time is monitored in both cases after either the pump or helium gas cylinder is isolated. In our tests, the pressure changed less than 6 Pa for both vacuum and pressurized tests. The duration of the tests were approximately 3 h.



(a) Condensation/Evaporation images



(b) Volume vs time

Fig. 8. Results from an evaporation/condensation experiment with liquid hydrogen in the 10 mm Al cell. Images 1–4 in show condensation while 5–8 depict evaporation. The volume of the liquid is calculated through image processing and shows two distinct evaporation zones where the observed rate from zone 2 is 3 times of that from zone 1.

2.8. Imaging

The imaging setup is detailed in a separate manuscript [15] and only a brief overview is provided here. Once the sample holder was inserted, the cryostat height was adjusted such that the center of the beam passed through the center of the test cell. Thermal neutrons (≈ 25 meV) penetrate the aluminum wall of the cryostat and interact with the test cell and its contents. The low neutron energy is estimated to increase the temperature of liquid hydrogen by < 1 μ K and is unlikely to influence phase change. A 20 μ m Gadolinium sulfide film was used as a scintillator and was placed downstream of the neutron beam. The scintillator is essentially a screen that emits visible (green) light after being excited by a neutron flux. The intensity of emitted light directly correlates to the density of neutron flux. The emitted light was captured by an Andor NEO sCMOS camera with a PK-13 extension tube. The contrast in the acquired neutron image was governed by neutron counting

statistics. Slower shutter speeds resulted in higher contrast between the bulk liquid and vapor but increase blur at the liquid–vapor interface during phase change. For the phase change rates tested (50 μ g/s to 250 μ g/s), the best trade off was achieved with a 10 s image integration time.

3. Operating Procedure

3.1. Dry tests with no visualization

“Dry” tests refer to thermal cycling experiments with an evacuated test cell. These were necessary to characterize the heat transfer mechanism between the heater and test cell of the system prior to introduction of hydrogen or methane. It also enables an estimation of the characteristic thermal response time. The test cells were thermally cycled by varying the heater setting and the transient response of the system was

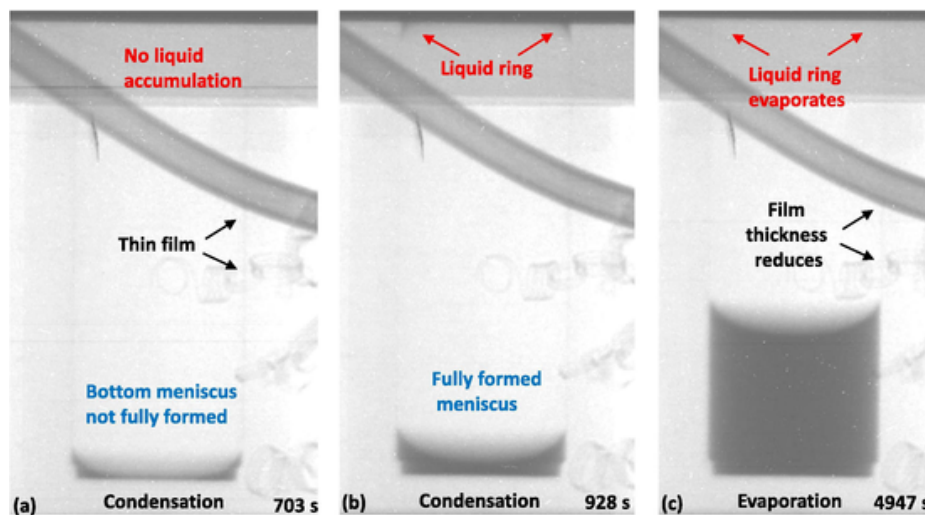


Fig. 9. Images from Methane Run 2. A thin liquid film forms at the onset of condensation (a). The liquid ring at the top corner appears only after the bottom meniscus is fully formed during condensation (b). At the onset of evaporation, the liquid ring readily evaporates and the film thickness reduces (c).

recorded using the temperature sensors mounted on the outer wall of the test cell. Fig. 5 shows a typical dry test using the 10 mm Al cell. The temperature of the heater was rapidly increased by approximately 10 K, the system was allowed to equilibrate and then temperature was lowered again. The temperature data were logged every second.

3.2. Wet tests with visualization

Prior to introduction of cryogen vapor, the heater was set to a temperature approximately 1 K higher than the saturation temperature of the preset vapor pressure. This ensured that vapor did not immediately condense upon entering the test cell. For the hydrogen tests, the manifold (Fig. 4) was connected to a hydrogen generator that delivers gas at approximately 1500 kPa. P1 and P2 are Mensor pressure transducers models CPG 2500 and DPG 15000, respectively. The uncertainty in pressure is 0.01% of the reading. For the methane tests, a compressed gas cylinder was instrumented with a Paroscientific model 745 pressure transducer, regulators and shutoff valves such that the methane pressure can be reduced to approximately 1500 kPa similar to hydrogen. In both methane and hydrogen tests, vapor was initially flowed freely into the manifold by opening the inlet. V3 and V4 are initially closed and the vapor exits through the atmospheric vent. The pressure was monitored by P2 and was reduced to the preset value (between 80 kPa to 250 kPa) using NV1. When the desired pressure was obtained, V3 was opened and vapor was allowed to flow into the test cell. The final adjustments were made using NV3 and P1. Hence, the vapor was constantly being vented to attain stable vapor pressure in the test cell. T1 and T2 allowed for isolating the test cell from the gas manifold for sample holder insertion/removal and enabled monitoring either the manifold or test cell vapor pressure as necessary. When the preset pressure was close to, or less than atmospheric pressure, the vapor was vented via the vacuum pump instead. Once the desired pressure setpoint was attained, the cryostat heater temperature was then decreased to between 0.5 K to 4 K below saturation. The vapor begins to condense into the test cell and was visualized in real time. Once a sufficient amount of liquid had condensed, the temperature was increased above saturation to begin evaporation. The evaporation rates are too low to result in nucleate boiling. During the tests, we attempted to keep the pressure variation as low as possible by actively adjusting NV3. The variation in vapor pressure was less than 0.5 kPa during steady phase change.

A typical test run consists of one complete condensation/evaporation cycle. For every run conducted, images were captured every 10 s while pressures (P1-P3) and temperatures (test cell outer wall and cryostat heater) were logged every 1 s. In the hydrogen tests, the heater

temperature was used as a trigger to initiate condensation and evaporation while the vapor pressure was held constant. However, in the methane tests, heater temperature was held constant and pressure was used as a phase change trigger. This is because at typical liquid methane temperatures, the heat transfer was much slower and temperatures take almost 3 times as long to reach steady state than for the case of liquid hydrogen. This is due to a combination of the change in material properties and additional contact resistances in the sample holder setup.

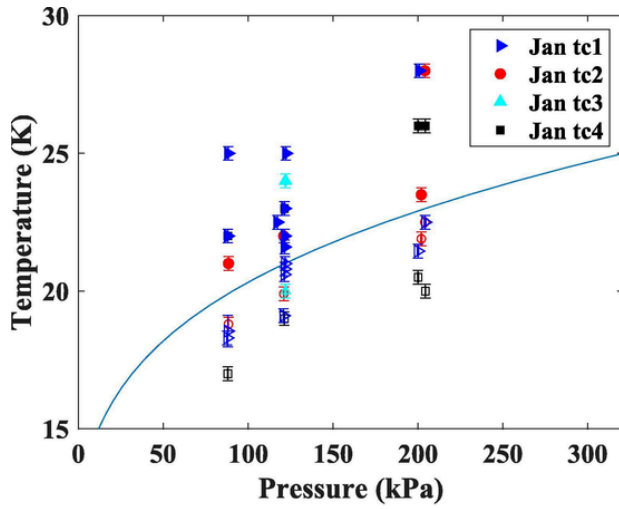
4. Analysis and Discussion

4.1. Heat Transfer

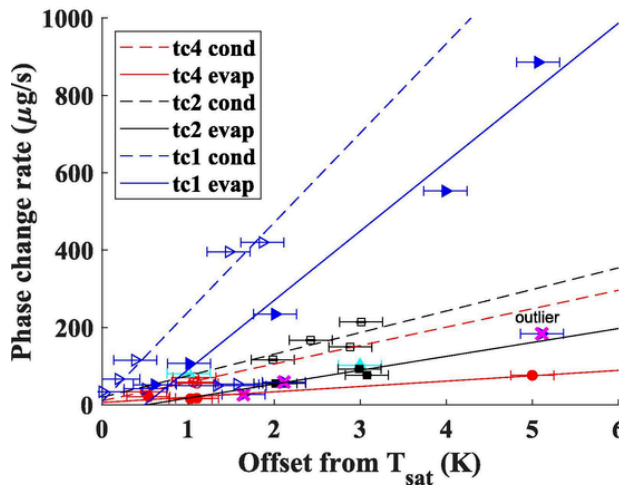
The contact area between the copper heater block and the bottom-most radiation baffle was approximately 1 mm wide. The lower radiation baffles on the sample holder were spring loaded such that they make contact with the copper heater block when fully inserted into the cryostat. However, this contact was not perfect and the amount of helium transfer gas could not be measured in the initial hydrogen experiments. As a result, the thermal contact resistance between the lower radiation baffle and the copper heater block presumably changes with each test configuration. Further, contact resistances also exist at every solid–solid interface. In order to accurately capture the thermal response, a transient thermal transport model was constructed. Contact resistances at solid–solid contacts were then determined by tuning the model to match the dry test results. The model suggests that the dominant heat transfer mechanism is by conduction. Modeling the helium as a stationary solid with properties of the vapor (essentially removing convection) changes the temperatures by less than 100 μ K confirming that heat transfer by convection is negligible [28]. The tuned model enables the calculation of inner wall temperature distribution from discrete outer wall temperature measurements. Details on the model and resulting values of contact resistances are published elsewhere [28].

4.2. Interface curvature and contact angle

Based on the curvature of the liquid–vapor interface in cylindrical cells, the contact angle could be determined. Initial estimates from preliminary tests (without accurate pressure or temperature control) indicated a 10° contact angle for liquid hydrogen. Subsequently, this estimation was improved using the conical cell with a 10° transition zone. If the contact angle was indeed 10° , the interface in the transition zone would be flat. Although visual inspection suggests the interface is flat, image processing revealed an angle between 10° and 2° (Fig. 6). Using



(a) Test conditions mapped on a saturation curve



(b) Departure from saturation temperature

Fig. 10. A summary of hydrogen test conditions are shown relative to the saturation curve (a). While departure from saturation results in increased phase change rate, the results also show a size and material dependence (b). The solid markers represent evaporation while the hollow markers represent condensation in both figures. In Fig. (b), linear fits to the condensation datapoints are represented by dashed lines while linear fits to evaporation datapoints are shown by solid lines. The evaporation rates are consistently lower than the condensation rates for the same temperature offset; i.e. slope of the dashed lines are larger than the corresponding solid lines. Data from tc1 where the meniscus was close to the 10° transition region is not included in the linear fit and are marked as outliers. Refer Table 2 for tc code.

an adaptive threshold and iterative matching to the Young–Laplace equation, the estimation was improved and the contact angle was estimated to be 0° to 4° [29]. Improving upon this further, a new “optical density” method [15] revealed that there exists a thin film of liquid that wicks up the side walls of the test cell. The optical density method involves normalizing the neutron images of the liquid with images of empty cell and then subtracting the background noise (with the beam turned off). This results in an “optical density” image where each pixel intensity is correlated to the distance the neutron traveled through the liquid. Fig. 7 shows a typical optical density image for hydrogen where the intensity increases with transmission distance. However when the region above the meniscus is scanned, the optical density profile shows two distinct peaks and the central value is not zero. This suggests that a thin liquid film exists on the inner wall providing strong evidence that both liquid hydrogen and methane are most likely perfectly wetting flu-

ids with a contact angle of 0° . The film thickness measurement is detailed in Section 4.5.

4.3. Phase change rate analysis

Sample images from a condensation/evaporation test using the 10 mm aluminum cell (Tc4) is shown in Fig. 8. Images 1–4 depict evaporation while images 5–8 depict condensation. The neutron images are post-processed to determine the evaporation/condensation rates using two approaches: (1) interface tracking and (2) optical density. The interface tracking method locates the meniscus, fits a Young–Laplace curve and then calculates the liquid volume in the region below the fitted interface. The optical density based volume measurement involves calculating the transmission distance from every pixel in the image. The transmission distance is converted into a volume using the pixel area and the individual pixel volumes are added up to obtain the total volume. The uncertainty in volume determination from interface tracking is about 6 % greater than the uncertainty in the optical density method. Furthermore, the interface tracking method can only be used when a fully formed meniscus is present. During the initial start and end of the tests, liquid is present only in corners. This volume is easily measured using the optical density method but not with the interface tracking method. A detailed comparison is available in [15]. Only the optical density data is shown in Fig. 8(b). Phase change rates for all other test cells/runs are not shown here but are available in the accompanying data repository [16].

The condensation and evaporation zones are delineated in Fig. 8(b). There appears to be two separate evaporation zones with two distinct rates even though there was no change in the pressure or temperature during the evaporation process. This suggests the presence of additional liquid outside the field of view. A very strong possibility was that liquid could condense at the top corner. This liquid pool likely forms “ring” at the top corner with 2 more contact lines in addition to the bottom meniscus. Out of the 3 contact lines in zone 1 the contribution from only one of them is captured in Fig. 8(b). If the top liquid ring evaporates readily during the first evaporation zone and was completely depleted by the start of the second zone, the slope of the line from the second zone is only from one contact line. The observed rate from zone 2 is approximately 3 times that of zone 1. However, the total evaporation rate is expected to be constant since there was no change in either temperature or pressure between the zones. This observation is a strong indication that the evaporation rate must scale with the number of contact lines (2 at the top and 1 at the bottom).

During the experiments with methane, the camera was intentionally zoomed out to verify the “top ring” hypothesis. The images reveal a liquid meniscus encircling the top corner between the test cell and flange (Fig. 9). This ring does not form at the onset of condensation but rather accumulates only after the bottom meniscus is fully formed. The ring exists throughout the condensation zone and readily evaporates at the onset of evaporation in zone 1 confirming the previous hypothesis.

Fig. 10(a) shows the different test conditions (temperature and pressure) in the hydrogen tests overlayed on the saturation curve. The temperature shown here corresponds to the S2 sensor on the test cell. At any point on the saturation line, net phase change is zero. To achieve condensation, the operating point must be below the curve and vice versa for evaporation. While it is evident that phase change rate increases with deviation from the saturation line, there are other factors that effect the rate such as container material and geometry. To elucidate, the temperature deviation from the equilibrium saturation line is shown as a function of the phase change rate in Fig. 10(b). Data with different test cells are color coded. The solid lines are linear fits to evaporation data while dashed lines represent condensation. The slopes of the lines increase with increasing test cell diameters, i.e tc1 (30 mm) > tc2 and tc4 (10 mm). The rates with tc2 (SS 316) are greater than the rates with tc4 (Al 6061) suggesting a wall material dependence despite

the same size. Additionally, evaporation rates are consistently lower than condensation for the same temperature deviation from saturation. This suggests that the condensation area is most likely larger than evaporation area; corroborated by the existence of the micro-scale thin film during condensation. The thin film effectively increases the surface area suggesting that condensation scales with area. In contrast, Fig. 8 (b) suggested that evaporation rate scales with the number of contact lines as described earlier. The other possible explanation for the inequality of evaporation and condensation rates for the same degree of equilibrium departure is an inequality of resistance to the phase change process at the interface which is characterized by phase change coefficients. It is common to assume that the evaporation coefficient is equal to the condensation coefficient but recent studies have suggested this may be an incorrect assumption [30]. Hence, it is also possible that the condensation coefficient is greater than the evaporation coefficient for liquid hydrogen.

4.4. Thin film analysis

From the central offset in Fig. 7, the film thickness of the liquid could be estimated using the Beer–Lambert law (Eq. 1) [15]. The film thickness in Fig. 7 is approximately $9.8 \pm 3.4 \mu\text{m}$. The resolution is limited by neutron counting statistics and image integration time. Although the optical density technique provides the ability to measure film thicknesses even lower than the optical resolution of $14 \mu\text{m}$, it is sensitive to changes in vapor density. To obtain a resolution of $3.4 \mu\text{m}$, the images are first normalized to an image of the empty evacuated cell.² During the calculation of film thickness, the attenuation in the vapor must be accounted for. To characterize this, the previously evacuated cell was imaged continuously as vapor was slowly introduced. The measured vapor pressure is converted to density using the ideal gas equation. The attenuation coefficient is determined using Eq. 1. The relationship between the attenuation coefficient and vapor density was found to be linear (Fig. 11). This enables accurate calculation of film thickness even when there are changes in vapor attenuation as a result of density/pressure variations.

A micro-scale liquid film formed on the walls of the test cell within the first 10 s of condensation testing. The thin film is observed in both hydrogen and methane but is more pronounced in methane due to a higher neutron attenuation. The film thickness is spatially uniform on the side walls but varies with time depending on the phase change rate. To elucidate, two methane tests are used as examples. Fig. 12(a) and 12 (c) represent the volume and film thickness during run 2; a slow condensation process followed by rapid evaporation. Here the condensation process is slow and steady during which the film thickness remains essentially constant. When evaporation is initiated, the film thickness quickly reduces to a negligible value. Figs. 12(b) and 12(d), represent the volume and film thickness during run 3; a rapid condensation process followed by slow evaporation. Here, the film thickness increases instantly to a value almost $10 \mu\text{m}$ higher than the previous run. When a slow evaporation process is initiated, the film thickness drops but at a much slower rate.

The liquid most likely condenses on the thin film condensate first and then drains due to gravity to form a meniscus at the bottom. Simultaneously, the condensed liquid film also “wicks up” to form a meniscus at the top corner. The top ring does not form instantly at the start of condensation. It appears to form only after the bottom meniscus is fully developed (Fig. 9). This is due to a delay in the thermal response of the stainless steel flange which initially inhibits condensate buildup at the top corner. During evaporation, the top ring evaporates readily.

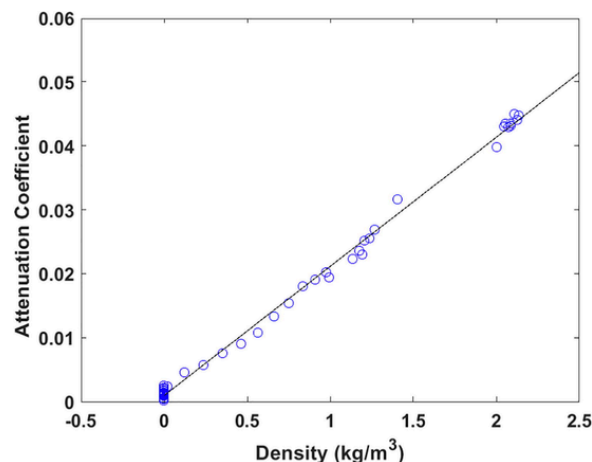


Fig. 11. The variation in the attenuation coefficient with hydrogen vapor density was characterized by imaging an evacuated cell as gas is slowly introduced into the cell.

4.5. Archival of test data

A complete set of raw (images, temperatures and pressures) and processed data (phase change rates, film thicknesses, etc) are not listed here for brevity but is available on the data repository [16]. The data is grouped per test campaign (‘Jan’ for hydrogen and ‘Sept’ for methane) and test cell (‘tc1-4’). Data from each run consists of images taken every 10 s along with pressure and temperature data taken every 1 s. In order to aid in correlation, the two separate data streams are combined for each test run. The avg temperatures and pressures during the 10 s interval are calculated and embedded directly into the image. A tabulated version is also available. In addition to temperature and pressure data, the tabulated data also contains liquid volume, film thickness and the meniscus location as a function of time. Phase change rates can be calculated from the volume vs time data. The publicly available data are intended to serve as a benchmark for future investigations.

5. Summary and Conclusion

The cryo-neutron phase change experiments conducted at NIST are detailed here and a discussion of experimental results are provided. In the experiments neutron imaging is used as a visualization tool to capture the location and shape of condensed liquid inside cylindrical opaque metallic containers. These are first known images of steady phase change in liquid hydrogen and methane. Tests were conducted in cylindrical containers of various sizes. A conical cell with a 10° transition was also tested. Cryogenic vapor (H_2 and CH_4) was introduced into the test cell after using a custom manifold. Through accurate control of temperature and pressure, a wide variety of phase change rates were obtained. The results are summarized below:

- Preliminary proof-of-concept images suggested a 10° contact angle but enhanced image analysis of subsequent experiments resulted in an updated estimate of 0° to 4° . Further, using the optical density analysis described here, the signal to noise ratio could be significantly improved. By enhancing the pixel intensities rather than the spatial resolution, a thin micro-scale liquid film was observed on the test cell walls. The condensed liquid also forms a “ring” at the top corner. This suggests that both liquid hydrogen and methane are most likely perfectly wetting fluids with a 0° contact angle.
- In the hydrogen experiments, the vapor was introduced at a constant, pre-set pressure and the temperature was altered from saturation to induce phase change. In the methane experiments, temperature was held constant and pressure was altered. Due to

² If normalized to an image of a vapor filled cell, the measured film thickness must be corrected for any deviation in vapor density from the original image

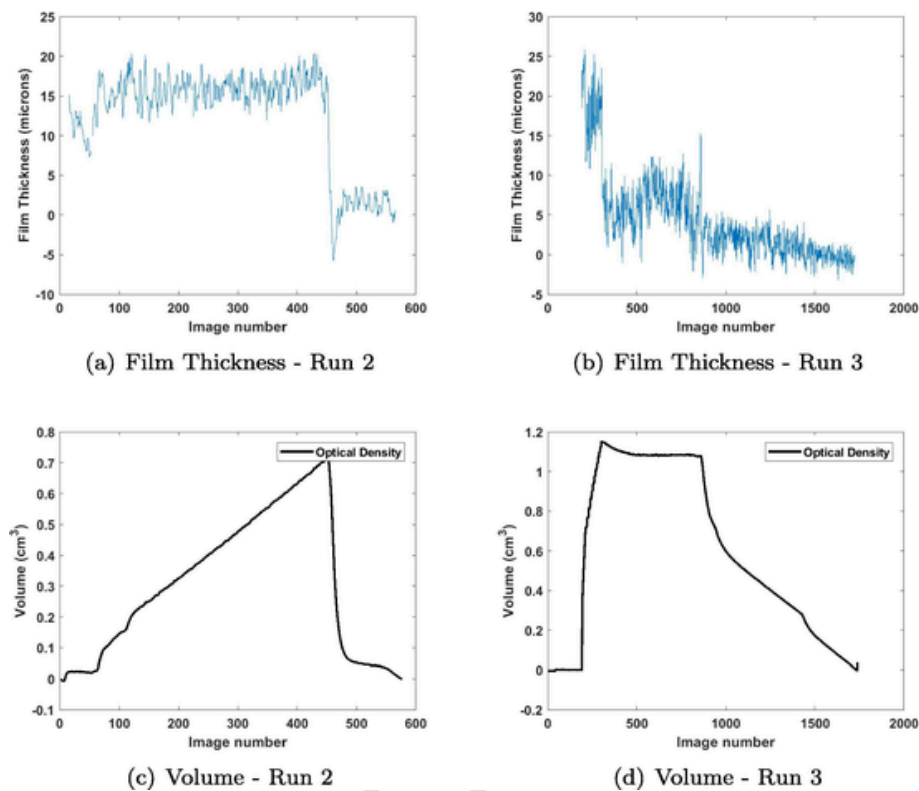


Fig. 12. Data from Methane - Run 2 are shown on the left: (a) film thickness and (c) volume. Data from the Methane - Run 3 is shown on the right: (b) film thickness and (d) volume. In both cases, film thickness is variation correlates with variations in phase change rates. Higher condensation rates result in increased film thickness. higher evaporation rates result in immediate depletion of the film. The error in film thickness is approximately $3.4\mu\text{m}$.

the slow thermal response at methane saturation temperatures (100 K). In general, the ability to control temperature and pressure in the methane experiments is more difficult due to this slow response.

- Measured rates of phase change depend on the magnitude of offset from saturation, test cell geometry and material. Rates increase with increase in temperature offset from saturation and size of container. In the case of hydrogen, for the same magnitude of temperature offset, the condensation rates are consistently greater than the evaporation rates. Condensation rate scales with surface area (r^2) while evaporation rate scales with the number and length of contact lines (r).
- A micro-scale thin film always exists during condensation. The film thickness decreases during evaporation and the magnitude of the decrease depends on the evaporation rate.

To the authors' best knowledge this is the first known study where controlled phase change of cryogenic propellants were systemically investigated with neutron imaging. Visualization of the meniscus enables an accurate determination of the phase change rates and measurement of adsorbed film thickness. The data generated here is unique and offers unprecedented insight into the dynamics of cryogenic phase change. The data and subsequent analysis provided here are critical for cryo-storage stability of propellant tanks for future space missions as well as for terrestrial transport of liquid hydrogen. The data from the experiment is made available through a data repository [16] in hopes that they will serve as a benchmark for future experimental investigations or be used as data for model validation.

6. Disclaimer

Certain trade names and company products are mentioned in the text or identified in an illustration in order to adequately specify the ex-

perimental procedure and equipment used. In no case does such identification imply recommendation or endorsement by the National Institute of Standards and Technology, nor does it imply that the products are necessarily the best available for the purpose.

Declaration of Competing Interest

The authors declare that they have no known competing financial interests or personal relationships that could have appeared to influence the work reported in this paper.

Acknowledgement

This work was supported by an Early Stage Innovations Grant from NASA's Space Technology Research Grants Program (Grant #NNX14AB05G) and a Physical Sciences Informatics Grant from NASA's Physical Sciences Research Program (Grant #80NSS-C19K0160). Support for this work was also provided from the University of Cincinnati through startup funds and Michigan Technological University through the Department of Mechanical Engineering - Engineering Mechanics, the John F. and Joan M. Calder Professorship, and the Winnikow Fellowship. The NIST authors acknowledge Mr. Eli Baltic for assistance with the experimental setup and support from the U.S. Department of Commerce, the NIST Radiation and Physics Division, the Director's office of NIST, and the NIST Center for Neutron Research.

References

- [1] Zhang J, Fisher T.S, Ramachandran P.V, Gore J.P, Mudawar I. A Review of Heat Transfer Issues in Hydrogen Storage Technologies. *J Heat Transfer* 2005;127(12): 1391–9. <https://doi.org/10.1115/1.2098875>.
- [2] Domashenko A, Golovchenko A, Gorbatsky Y, Nelidov V, Skorodumov B. Production, storage and transportation of liquid hydrogen. Experience of infrastructure development and operation. *Int J Hydrogen Energy* 2002;27(7): 753–5. [https://doi.org/10.1016/S0360-3199\(01\)00152-5](https://doi.org/10.1016/S0360-3199(01)00152-5).

- [3] Panzarella C.H, Kassemi M. On the validity of purely thermodynamic descriptions of two-phase cryogenic fluid storage. *J Fluid Mech* 2003;484:41–68. <https://doi.org/10.1017/S0022112003004002>.
- [4] Panzarella C, Kassemi M. One-dimensional model of evaporation and condensation in the presence of a noncondensable gas with applications to cryogenic fluid storage. *Int J Heat Mass Transf* 2009;52(15–16):3767–77. <https://doi.org/10.1016/j.ijheatmasstransfer.2009.02.027>.
- [5] Alberts S.J, Srikanth P, Collicott S.H, Heister S.D. Experiment Design for Measuring Accommodation Coefficients for Modeling of Long-Duration Spaceflight Cryogenic Propellants. In: 13th International Energy Conversion Engineering Conference, American Institute of Aeronautics and Astronautics, Orlando, FL; 2015. <https://doi.org/10.2514/6.2015-4246>.
- [6] Alberts S.J, Srikanth P, Collicott S.H, Heister S.D. Numerical Approach to Measure Accommodation Coefficients for Long-Duration Spaceflight Cryogenic Propellants. In: 52nd AIAA/SAE/ASEE Joint Propulsion Conference, American Institute of Aeronautics and Astronautics, Salt Lake City, UT; 2016. <https://doi.org/10.2514/6.2016-4675>.
- [7] Srikanth P, Collicott S.H. Estimation of Thin-Film Contribution in Phase Change Calculations Involving Cryogenic Propellants. *J Spacecraft Rock* 2019;56(5): 1646–50. <https://doi.org/10.2514/1.A34495>.
- [8] Kassemi M, Kartuzova O. Effect of interfacial turbulence and accommodation coefficient on CFD predictions of pressurization and pressure control in cryogenic storage tank. *Cryogenics* 2016;74:138–53. <https://doi.org/10.1016/j.cryogenics.2015.10.018>.
- [9] Hartwig J, Rhys N, Clark J, Mercado M, LeClair A, Majumdar A. Test Data Analysis of the Vented Chill, No-Vent Fill Liquid Nitrogen CRYOTE-2 Experiments. *Int J Heat Mass Transf* 2021;167:120781. <https://doi.org/10.1016/j.ijheatmasstransfer.2020.120781>.
- [10] Statharas J.C, Venetsanos A.G, Bartzis J.G, Würtz J, Schmidtchen U. Analysis of data from spilling experiments performed with liquid hydrogen. *J Hazard Mater* 2000;77(1):57–75. [https://doi.org/10.1016/S0304-3894\(00\)00252-1](https://doi.org/10.1016/S0304-3894(00)00252-1).
- [11] Nakamichi K, Kihara Y, Okamura T. Observation of liquid hydrogen jet on flashing and evaporation characteristics. *Cryogenics* 2008;48(1–2):26–30. <https://doi.org/10.1016/j.cryogenics.2007.09.004>.
- [12] Hasan M, Lin C, Dresar N. Self-pressurization of a flightweight liquid hydrogen storage tank subjected to low heat flux. *Tech Rep NASA TM* 1991;103308.
- [13] Hastings L.J, Flachbart R.H, Martin J.J, Hedayat A, Fazah M, Lak T, et al. Spray Bar Zero-Gravity Vent System for On-Orbit Liquid Hydrogen Storage. *Tech Rep NASA TM* 2003;212926.
- [14] Bellur K, Médici E.F, Kulshrestha M, Konduru V, Tyrewala D, Tamilarasan A, et al. A new experiment for investigating evaporation and condensation of cryogenic propellants. *Cryogenics* 2016;74:131–7. <https://doi.org/10.1016/j.cryogenics.2015.10.016>.
- [15] Bellur K, Konduru V, Médici E.F, Hussey D.S, Jacobson D.L, LaManna J.M, et al. Visualization of the evaporation and condensation phenomena in cryogenic propellants. *J Flow Visual Image Process* 2016;23(1–2). <https://doi.org/10.1615/JFlowVisImageProc.2017020115>.
- [16] Bellur K. Data from cryo-neutron phase change experiments with LH2 and LCH4. *Mendeley Data* 2021. <https://doi.org/10.17632/z5zc7kk76g.1>.
- [17] Brenizer J.S. A Review of Significant Advances in Neutron Imaging from Conception to the Present. *Phys Proc* 2013;43:10–20. <https://doi.org/10.1016/j.phpro.2013.03.002>.
- [18] Strobl M, Manke I, Kardjilov N, Hilger A, Dawson M, Banhart J. Advances in neutron radiography and tomography. *J Phys D: Appl Phys* 2009;42(24):243001. <https://doi.org/10.1088/0022-3727/42/24/243001>.
- [19] Sears V.F. Neutron scattering lengths and cross sections. *Neutron News* 1992;3(3):26–37. <https://doi.org/10.1080/10448639208218770>.
- [20] Dewanckele J, De Kock T, Fronteau G, Derluyt H, Vontobel P, Dierick M, et al. Neutron radiography and X-ray computed tomography for quantifying weathering and water uptake processes inside porous limestone used as building material. *Mater Charact* 2014;88:86–99. <https://doi.org/10.1016/j.matchar.2013.12.007>.
- [21] Kang M, Bilheux H.Z, Voisin S, Cheng C.L, Perfect E, Horita J, et al. Water calibration measurements for neutron radiography: Application to water content quantification in porous media. *Nucl Instrum Methods Phys Res, Sect A* 2013;708: 24–31. <https://doi.org/10.1016/j.nima.2012.12.112>.
- [22] Perfect E, Cheng C.L, Kang M, Bilheux H.Z, Lamanna J.M, Gragg M.J, et al. Neutron imaging of hydrogen-rich fluids in geomaterials and engineered porous media: A review. *Earth Sci Rev* 2014;129:120–35. <https://doi.org/10.1016/j.earscirev.2013.11.012>.
- [23] Bazylak A. Liquid water visualization in PEM fuel cells: A review. *Int J Hydrogen Energy* 2009;34(9):3845–57. <https://doi.org/10.1016/j.ijhydene.2009.02.084>.
- [24] Kramer D, Zhang J, Shimoi R, Lehmann E, Wokaun A, Shinohara K, et al. In situ diagnostic of two-phase flow phenomena in polymer electrolyte fuel cells by neutron imaging. *Electrochim Acta* 2005;50(13):2603–14. <https://doi.org/10.1016/j.electacta.2004.11.005>.
- [25] Kihm K, Kirchoff E, Golden M, Rosenfeld J, Rawal S, Pratt D, et al. Neutron Imaging of Alkali Metal Heat Pipes. *Phys Proc* 2013;43:323–30. <https://doi.org/10.1016/j.phpro.2013.03.038>.
- [26] J.M. Cimbala, J.S. Brenizer, A.P.-Y. Chuang, S. Hanna, C. Thomas Conroy, A.A. El-Ganayni, D.R. Riley, Study of a loop heat pipe using neutron radiography, *Applied Radiation and Isotopes* 61 (4) (2004) 701–705. doi:10.1016/j.apradiso.2004.03.104.
- [27] Bellur K, Médici E, Allen J, Hermanson J, Tamilarasan A, Hussey D, et al. Neutron Radiography of Condensation and Evaporation of Hydrogen in a Cryogenic Condition. *J Heat Transfer* 2015;137(8):80901. <https://doi.org/10.1115/1.4030442>.
- [28] Bellur K, Médici E.F, Hermanson J.C, Choi C.K, Allen J.S. Determining solid-fluid interface temperature distribution during phase change of cryogenic propellants using transient thermal modeling. *Cryogenics* 2018;91:103–11. <https://doi.org/10.1016/j.cryogenics.2018.02.009>.
- [29] Bellur K, Konduru V, Kulshrestha M, Tyrewala D, Médici E, Allen J.S, et al. Contact Angle Measurement of Liquid Hydrogen (LH2) in Stainless Steel and Aluminum Cells. *J Heat Transfer* 2016;138(2). <https://doi.org/10.1115/1.4032232>. Feb.
- [30] Montazeri K, Hao S, Abdolhosseini Qomi M.J, Won Y. Molecular Dynamics Investigation of Liquid and Vapor Interactions Near an Evaporating Interface: A Theoretical Genetics Perspective. *Adv Theory Simul* 2020;3(7):2000017. <https://doi.org/10.1002/adts.202000017>.